# Impact of Moisture on Photoexcited Charge Carrier Dynamics in Methylammonium Lead Halide Perovskites

Zhaoning Song,[#] Niraj Shrestha,[#] Suneth C. Watthage, Geethika K. Liyanage, Zahrah S. Almutawah, Ramez H. Ahangharnejhad, Adam B. Phillips, Randy J. Ellingson, and Michael J. Heben[*]

Wright Center for Photovoltaics Innovation and Commercialization, Department of Physics and Astronomy, University of Toledo, 2801 West Bancroft Street, Toledo, Ohio 43606 United States

S *Supporting Information*

ABSTRACT: Organic−inorganic metal halide perovskites are notoriously unstable in humid environments. While many studies have revealed the morphology and crystal structure changes that accompany exposure to humidity, little is known about changes to the photophysics that accompany the degradation process. By combining in situ steady-state and time-resolved photoluminescence with Hall effect measurements, we examined the changes in the photoexcited carrier dynamics for methylammonium lead iodide ($MAPbI_3$) and bromide ($MAPbBr_3$) films exposed to nitrogen gas containing water vapor at 80% relative humidity. The changes in the photophysics of $MAPbI_3$ interacting with water follow a four-stage process, consisting of surface passivation, free electron doping, interfacial hydration, and bulk hydration. In contrast, $MAPbBr_3$ exhibits only features associated with the first two stages, which occur at a faster rate. Our results elucidate the degradation mechanisms of perovskite films in high humidity from the perspective of the photophysics, providing insights for how humidity affects the stability of the perovskite materials.
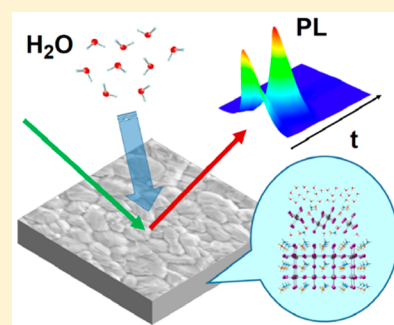
Solar cells based on organic−inorganic metal halide perovskites have drawn substantial attention in the past few years due to the high power conversion efficiencies of >23%[1] in combination with easy material synthesis, low-cost device fabrication, and low environmental impacts.[2−10] With intense research effort directed at continuing to improve device performance, perovskite solar cells are now being considered as promising rivals to the more established photovoltaic (PV) technologies, such as crystalline silicon and some thin films (e.g., CdTe and $CuIn_{1-x}Ga_xSe_2$).[11,12] While low-cost processes for fabrication of perovskite modules have been designed,[13,14] commercial deployment is hindered by performance degradation during operation, and several fundamental issues concerning the perovskite material and device stability remain unanswered.[15] Without addressing these stability issues, the full potential of this promising PV technology cannot be realized. Therefore, searching for the origins of instabilities and developing strategies to circumvent them have become key research goals in the field of perovskite PV research.[16−20]

The conventional perovskite materials, with methylammonium lead iodide ($MAPbI_3$) and bromide ($MAPbBr_3$) serving as prototypes, are notoriously unstable in ambient environments. Although the underlying degradation mechanisms are far from completely understood, preliminary studies have identified environmental factors such as humidity,[21,22] oxygen,[23−25] light,[26−28] and heat[29,30] and intrinsic device factors such as the electrode metal migration/reaction[31−33] and ionic defects in the perovskite material itself.[34,35] These mechanisms operate in parallel to deteriorate device performance. Among these, humidity has been demonstrated as the most aggressive cause of instability in materials and devices due to the formation of the intermediate hydrated perovskite phases such as $CH_3NH_3PbI_3·H_2O$ and $(CH_3NH_3)_4PbI_6·2H_2O$,[36−38] which subsequently decompose into solid-state PbI_2 and volatile gases (e.g., HI and CH_3NH_2).[39] While many studies have revealed that morphology and structure both change in perovskite films after exposure to humidity,[40−43] little is known about the changes in the photophysics that accompany water-induced degradation.

Most recently, studies on luminescence properties of hybrid perovskite films in the presence of dry nitrogen and oxygen atmospheres revealed diverse photophysical phenomena related to the nature of instabilities of perovskites.[44,45] These findings opened an avenue to investigate the correlation between the formation of sub-band-gap defect states and the stability of perovskite materials. In this Letter, we investigate the photoexcited carrier dynamic processes of $MAPbI_3$ and $MAPbBr_3$ thin films under humidity using in situ steady-state and time-resolved photoluminescence (PL and TRPL, respectively) measurements in combination with Hall effect measurements. Our results reveal the underlying photophysics that govern device performance degradation and allow definition of the performance boundaries for perovskite solar cell operation in humid environments.

To characterize the optoelectronic properties of pristine $MAPbX_3$ (X = I or Br) samples, we prepared perovskite films
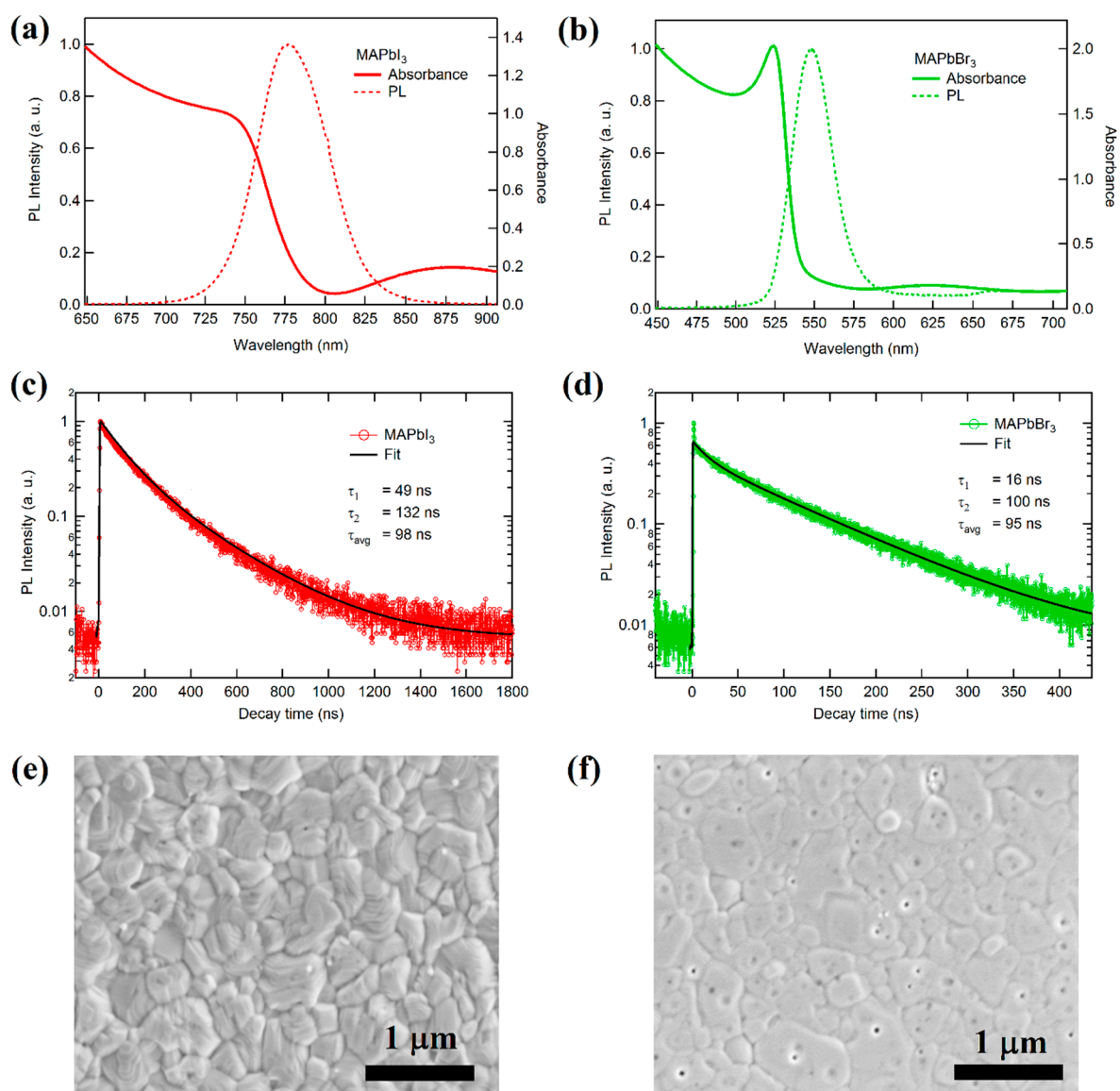
Figure 1. PL and OA spectra of pristine (a) MAPbI$_3$ and (b) MAPbBr$_3$ films. TRPL decays of pristine (c) MAPbI$_3$ and (d) MAPbBr$_3$ films. SEM images of pristine (e) MAPbI$_3$ and (f) MAPbBr$_3$ films.

on soda-lime glass substrates in a nitrogen glovebox and immediately characterized their photophysics while limiting exposure to the air. Figure 1a shows optical absorbance (OA) and PL spectra of pristine MAPbI$_3$ films. The absorption band edge of 1.59 eV determined by the Tauc plot (Figure S1) is consistent with the PL emission centered at 776 nm (1.60 eV). A blue shift in the emission relative to the bulk emission from MAPbI$_3$ single crystals (~1.54 eV) is observed, which is typical for polycrystalline films. The blue shift was attributed to lattice deformation near the surface and grain boundaries in the past.[46,47] A recent study by Wenger et al. pointed out that carrier diffusion and reabsorption by the surface could be the main mechanism behind the blue-shifted PL.[48] In contrast to MAPbI$_3$, the OA signal for MAPbBr$_3$ films shows band-to-band as well as excitonic absorption features (Figure 1b).[49−51] The continuum band edge at 544 nm (2.28 eV) and the prominent excitonic absorption band at 525 nm (2.36 eV) were extracted by fitting the OA spectrum using the Elliott formula (Figure S2).[52,53] The excitonic binding energy was determined to be ~80 meV, consistent with the values

reported in the literature.[47,49] The PL emission was centered at 547 nm (2.27 eV), with a small Stokes shift from the continuum band edge due to vibronic relaxation of the perovskite crystal.[54]

Turning to the TRPL data, the average minority carrier lifetimes of the as-prepared MAPbI$_3$ (Figure 1c) and MAPbBr$_3$ (Figure 1d) samples are 98 and 95 ns, respectively. However, the details of the PL decay dynamics reveal different recombination behaviors. The MAPbI$_3$ film shows an initial fast decay time constant (τ_1) of 49 ns, which can be attributed to surface recombination, and a slower component (τ_2) of 132 ns that is related to recombination in the bulk. These values are typical for perovskite films with a smooth surface morphology (Figure 1e) and also for certain single crystals.[47] The MAPbBr$_3$ film exhibits a faster initial decay with a time constant of 16 ns, likely due to the presence of surface defects (Figure 1f). However, the slow component (~100 ns) dominates the decay process with ~95% yield (Table S1), indicting good crystallinity in the bulk. X-ray diffraction measurement (Figure S3) confirmed that the perovskite films used for this study
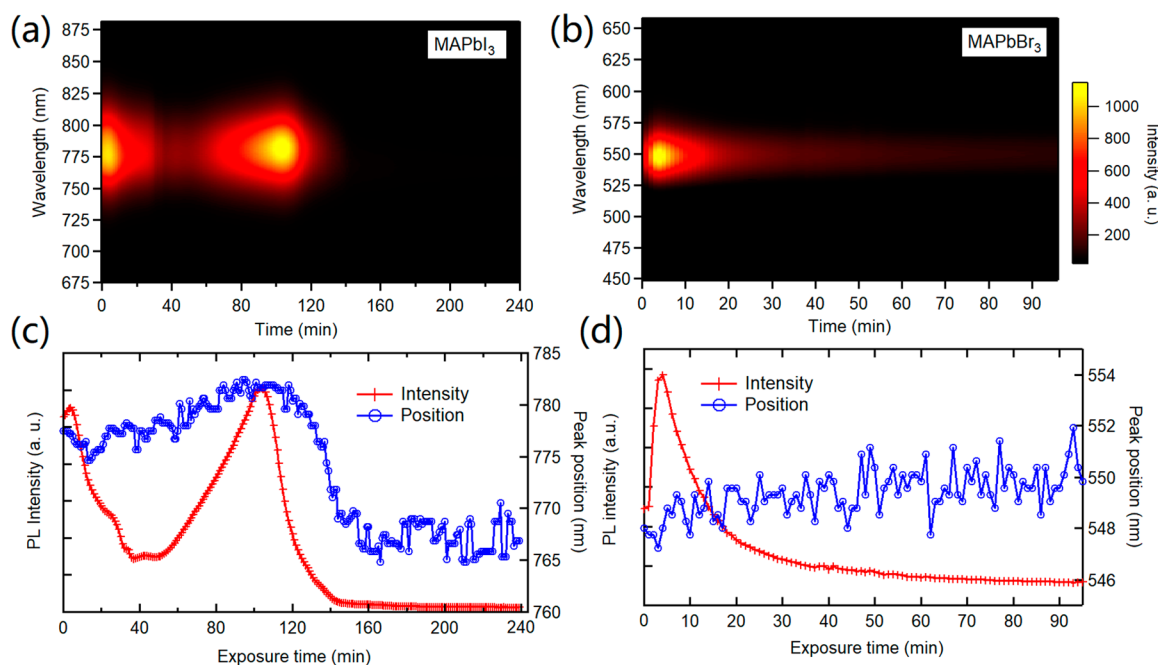
Figure 2. PL evolution images of (a) MAPbI$_3$ and (b) MAPbBr$_3$ as a function of time after exposure to 80% RH. PL emission peak intensity and position of (c) MAPbI$_3$ and (d) MAPbBr$_3$ as a function of the exposure time.
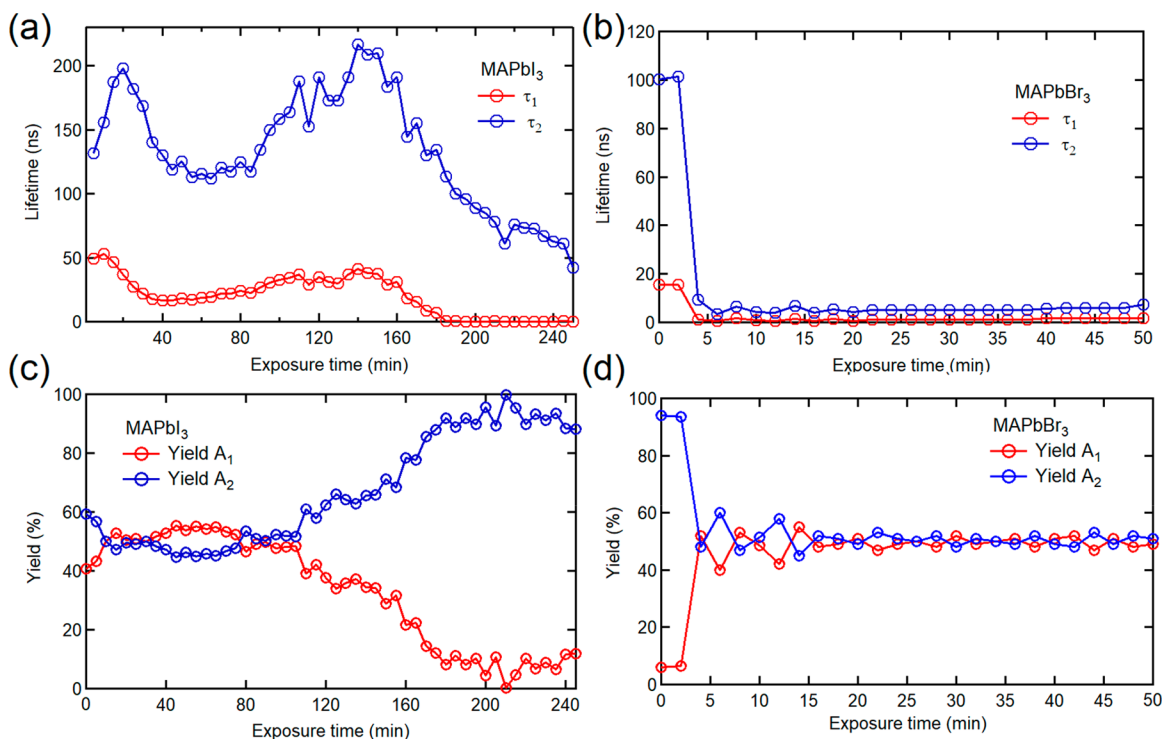

Figure 3. Evolution of TRPL time constants and yields of (a,c) MAPbI$_3$ and (b,d) MAPbBr$_3$ as a function of time after exposure to 80% RH.

were phase-pure with good crystallinity and are representative of high-quality solution-processed perovskite films.

The photophysics of the perovskite films were then examined during exposure to a flowing nitrogen gas containing moisture at a relative humidity (RH) of 80 ± 5% (~25 mbar of H$_2$O at 300 K) through an in-house-built environmental chamber (Figure S4). The control experiments under dry nitrogen flow were performed. In agreement with previous reports,[44,45] we observed lower PL intensities of the perovskite

films in nitrogen compared to those in air. However, unlike the perovskite films under oxygen,[45] there were no significant changes due to laser illumination after monitoring PL signals of MAPbI$_3$ and MAPbBr$_3$ under nitrogen for up to 4 h (Figure S5), indicating decent photostability of the perovskite films under nitrogen. Figure 2a shows the evolution in PL emission from MAPbI$_3$ as a function of moisture exposure time. Data was collected at 1 min intervals using a charge-coupled device (CCD) camera, and three samples were studied for each
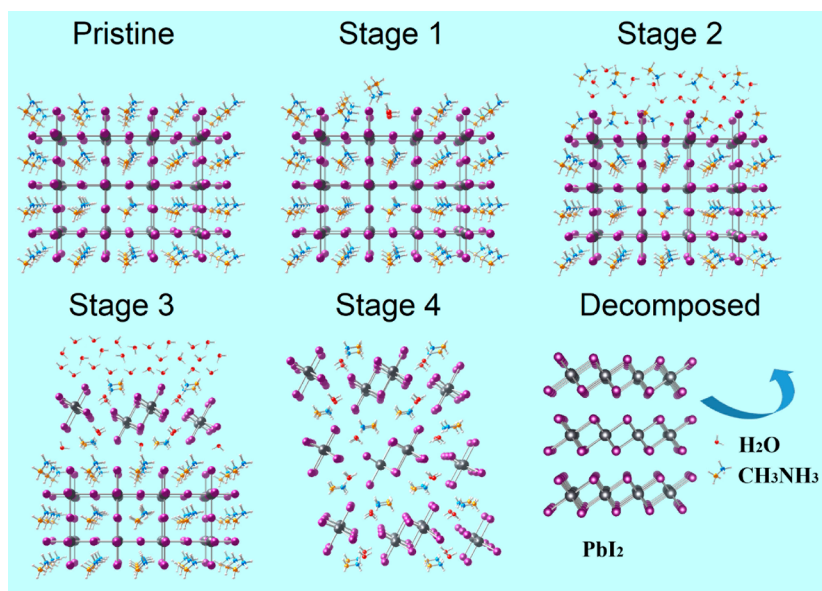
Figure 4. Schematic illustrations of the MAPbI$_3$ crystal structure evolution at the different stages of water exposure, including pristine MAPbI$_3$, water-assisted surface passivation (Stage 1), water induced n-type doping (Stage 2), formation of the monohydrated perovskite interface (Stage 3), conversion to the hydrate phase (Stage 4), and complete decomposition into PbI$_2$.

measurement to ensure statistically significant results (see the [Experimental Methods](#) section for details). Four distinct stages can be discerned. At early times, the PL intensity increases and peaks after ~4 min of humidity exposure (Stage 1). After this transient brightening, the PL emission suffers a deep decline and the intensity reaches a minimum after ~40 min (Stage 2). The drop of PL emission during the first two stages is partially reversible, which is consistent with the observation of the reversible drop of photocurrent in MAPbI$_3$ devices.[38] Surprisingly, after stabilizing, the PL emission begins to climb again after ~50 min and temporarily peaks after ~100 min with an intensity that is higher than that of the pristine film (Stage 3). Finally, the peak intensity gradually decreases to zero after ~140 min (Stage 4). In addition to the intensity variation, the PL peak position red shifts from 778 to 782 nm (8 meV) during the first three stages and then blue shifts to 765 nm (27 meV) during the last stage ([Figure 2](#)c).

In contrast, the PL from the MAPbBr$_3$ film underwent a two-stage evolution ([Figure 2](#)b). After initial transient improvement over the first ~5 min of exposure time (Stage 1), the PL emission showed a rapid exponential decay as time elapsed (Stage 2). However, a weak PL emission, with only ~10% of the highest intensity, was still observed after 5 h, indicating that a small portion of the perovskite film retained photoluminescent properties. Interestingly, the PL peak position of MAPbBr$_3$ was red-shifted after Stage 2 by only a few meV ([Figure 2](#)d). This suggests that a shallow defect level had formed that lowered the emission energy with respect to the band-to-band emission.

To better understand the changes in the photophysics that accompany the degradation processes, we measured the time evolution of the TRPL data from MAPbI$_3$ and MAPbBr$_3$ films while they were exposed to the same environmental conditions ([Figure 3](#)). The TRPL data was collected over 5 and 2 min time intervals for the MAPbI$_3$ and MAPbBr$_3$ films, respectively, to ensure sufficient signal for quantitative analysis. The data was well fitted by the following biexponential function

$$f(t) = C_1 \times \exp\left(-\frac{t}{\tau_1}\right) + C_2 \times \exp\left(-\frac{t}{\tau_2}\right)$$

where τ_1 and τ_2 are the fast and slow time constants of the decay and C_1 and C_2 are amplitudes. Yield percentages for the two time constants are calculated as $A_1 = C_1\tau_1/(C_1\tau_1 + C_2\tau_2)$ and $A_2 = C_2\tau_2/(C_1\tau_1 + C_2\tau_2)$.

[Figure 3](#)a,b shows the time evolution of the two time constants extracted from the MAPbI$_3$ and MAPbBr$_3$ data sets. The same general four-stage evolution that was observed in the steady-state PL data of MAPbI$_3$ is evident, as is the two-stage behavior for MAPbBr$_3$. Small changes in the timing of the stages are attributed to sample-to-sample variation, film inhomogeneity, gas flow, etc., but the data makes it clear that the photoexcited carrier dynamics are governed by the same mechanisms that control the steady-state PL behavior, as expected.

Consideration of the yields of the two time constants ([Figure 3](#)c,d), however, provides new insights. In the case of MAPbI$_3$, the yield ratio of A_2 to A_1 is close to 1 in both Stages 1 and 2 but increases dramatically as the perovskite hydration occurs. The increasing ratio (A_2/A_1) shows the improved surface passivation for the MAPbI$_3$ films. During Stages 3 and 4, A_2 (the slow component) becomes dominant, indicating that the surface defects were effectively passivated. However, the bulk film quality of MAPbI$_3$ is increased first (Stage 3) and then decreased (Stage 4) during the decomposition process. At the end of the experiment, the total PL intensity is low, but the volume of material that is still emitting is doing so with an effectively long lifetime. These findings are consistent with localized bright regions that have been reported in laser-beam-induced current measurements.[38] The findings for MAPbBr$_3$, however, are dramatically different. In this case, we see a ratio of A_2 to A_1 that is much greater than 1 initially, and it very quickly falls to ~1:1. This result reveals that the surface of MAPbBr$_3$ is very sensitive to water.

Combining the PL and TRPL results, we can develop a comprehensive picture of the water-induced changes in the

photoexcited carrier dynamics in MAPbI$_3$ and MAPbBr$_3$ films. Figure 4 illustrates the structural aspects of the four-stage evolution of MAPbI$_3$ in a humid environment as well as the initial and final products of the process. Generally, the pristine polycrystalline perovskite films of MAPbI$_3$ possess uncoordinated bonds on the surface and grain boundaries, and these can act as charge traps. When the perovskite film is first exposed to humidity (Stage 1, Figure 4), water molecules quickly form hydrogen bonds with uncoordinated I atoms at the surface, which suppresses nonradiative surface recombination.[55] Evidence for hydrogen-bonded water molecules in the inorganic Pb−I network were revealed by infrared spectroscopy work performed by Müller et al.[56] Interfacial ab initio molecular dynamics simulations[57,58] showed that a small concentration of water molecules can localize photoexcited electrons to the perovskite/water interface, decreasing electron−hole overlap and increasing the excited-state lifetime.[58] Therefore, we attribute the initial enhancement in PL intensity and photoexcited carrier lifetime to water-assisted surface passivation, which in turn leads to enhanced photocurrent generation in MAPbI$_3$ devices.[38]

When the water partial pressure is increased (Stage 2, Figure 4), water molecules start to form a continuous network that fully covers the perovskite surface. This water surface layer delocalizes the electron wave function in the perovskite crystal[58] and creates effective n-type doping by donating free electrons into the bulk. Moreover, water molecules contribute to high-frequency polar vibrations at the interface, which increases vibronic coupling.[58] As a result, nonradiative recombination of photoexcited carriers is accelerated, and both the PL emission intensity and minority carrier lifetime are decreased. A recent X-ray photoelectron spectroscopy study by Li et al. revealed that the Fermi level of MAPbI$_3$ is shifted from 0.85 to 1.41 eV above the valence band maximum after water molecules infiltrate the perovskite, demonstrating that embedded water acted as a strong n-type dopant.[59]

To probe the doping effect of water in the perovskite films, we measured electrical conductivity and the Hall voltage of perovskite films during humidity exposure (see the Experimental Methods section for details), and the effective donor density as a function of exposure time was calculated. Figure 5a shows the electron density change as a function of time exposed to humidity. For the MAPbI$_3$ film, the free electron density increased dramatically from ~10^{14} to ~10^{20} cm^{-3} in the period of ~4 to ~50 min (Stage 2). The increased free electron density, most likely appearing at the grain surfaces,[60] accelerated the recombination rate with holes and thus shortens the minority carrier lifetime. In fact, we have shown that water vapor can convert the photoactive MAPbI$_3$ in the perovskite/Si tandem solar cells into a semitransparent conductive material.[61,62] The rapid increase of conductivity of the perovskite film is consistent with the report by Müller et al.[56] Additionally, the water-induced n-type doping creates a donor energy level within the band gap of the perovskite (Figure 5b), leading to a slight red shift of the PL emission peak.

In Stage 3 (Figure 4), water vapor saturates on the surface of the perovskite crystal, hydroxide substitution on the halide lattice occurs, and CH$_3$NH$_3^+$ and I$^-$ species are released from the lattice.[57] This process weakens the bonding in the crystals and eventually dissolves the surface layer of the Pb−I framework. The dissolved Pb−I octahedra are then likely to combine with the organic species, forming an intermediate
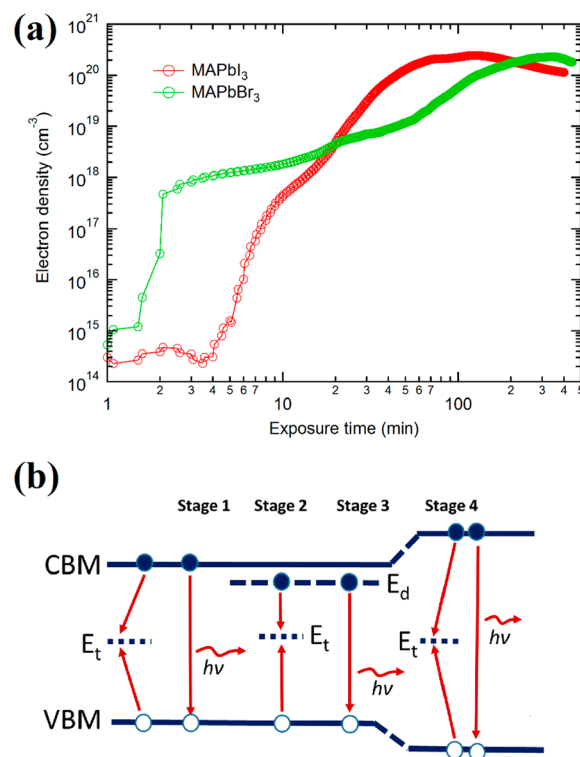

Figure 5. (a) Charge carrier density of MAPbI$_3$ and MAPbBr$_3$ as a function of time after exposure to 80% RH. (b) Illustration of charge carrier recombination pathways, including nonradiative, band-to-band, and donor-band recombination types in perovskite and hydrated perovskite.

low-dimensional hydrated perovskite layer that separates the bulk perovskite from the surrounding water. This monohydrate perovskite layer acts as a diffusion barrier that isolates the bulk perovskite crystal from surface water coating, effectively halting the free electron generation due to water doping. Moreover, the wide-band-gap (E_g = 3.1 eV) monohydrate perovskite layer effectively passivates the surface of the perovskite films, leading to a decreased surface/bulk (A_1/A_2) yield ratio for the lifetimes (Figure 3c). Once the free carrier density gradually saturates in the period of ~60 to ~100 min (Figure 5a), a small portion of the water molecules can infiltrate more deeply into the bulk perovskite, likely through grain boundaries, and start to passivate the grain boundary defects of the underlying perovskite crystals. As a result, nonradiative recombination was quenched while the PL intensity was enhanced (Figure 2c). Charge carriers excited in the bulk can survive for a longer time, leading to a significant increase in the bulk carrier lifetime from ~100 to ~200 ns (Figure 3c). This enhancement in the bulk perovskite optoelectronic properties is likely related to the improved device performance when perovskite solar cells are fabricated in a humid environment.[63−65]

While humidity is beneficial for defect passivation in the MAPbI$_3$ perovskite, excess exposure to humidity is detrimental to the perovskite due to the well-known hydration−decomposition process (Stage 4, Figure 4).[36−38] The high water chemical potential promotes complete transition from the perovskite phase into the monohydrated perovskite phase. The monohydrated phase is inactive to incident photons, and the absence of photogenerated charge carriers results in no PL response in the visible range. The weak PL signal observed here is possibly due to the remaining perovskite nanocrystals

,which likely exist in a dynamic equilibrium with the hydrated phases.[38,42] Additionally, the hydrated perovskite phase widens the band gap of the surface states of the perovskite by perturbing the interfacial band structure via surface deformation (Figure 5b),[66] leading to a blue shift of the PL emission peak (Figure 2c). This surface distortion is likely the initial step of structural reorganization toward the morphological destruction.[36] If the water−perovskite reaction proceeds, the hydrated perovskites will decompose permanently into solid-state PbI_2, while the volatile organic fragments are freed from the perovskite crystal (Figures S5 and S6).

In contrast to $MAPbI_3$, only the first two stages of the photophysical behavior are observed in $MAPbBr_3$ films. The water-assisted surface passivation (Stage 1, Figure 4) temporarily improves the optoelectronic quality of the $MAPbBr_3$, as with $MAPbI_3$, but this trend is quickly reversed due to water-induced n-type doping (Stage 2, Figure 4), which occurs much more rapidly. Thus, $MAPbBr_3$ is quickly turned into a photoinactive material. The latter process, analogous to Stage 2 of water−perovskite interaction, is accompanied by a red shift of PL emission due to n-type doping (Figure 2d). This degradation process likely occurs at a much faster rate due to the stronger ionic characteristic of the Pb−Br bond relative to the Pb−I bond, which makes charge injection easier compared with the I-based counterpart. Electrical resistance measurement shows rapid free electron injection, which increases the electron density of $MAPbBr_3$ from $\sim 10^{15}$ to $\sim 10^{18}$ within ~ 2 min of exposure to humidity (Figure 5a). Unlike $MAPbI_3$, water-induced degradation was identified on the surface only after exposing $MAPbBr_3$ films to humidity for 5 h (Figures S5 and S6). Therefore, the evolution processes related to the hydrated phases (Stages 3 and 4) are unlikely to be present in $MAPbBr_3$ in the time scale of the measurement. Because of the absence of the hydrated phases, $MAPbBr_3$ shows better structural stability than $MAPbI_3$ against humidity. However, water can deteriorate the device operation of $MAPbBr_3$ solar cells through the changing photophysics of the material.

In summary, we investigated the photoexcited charge carrier dynamics in $MAPbI_3$ and $MAPbBr_3$ films during exposure to humidity. We observed that the photophysical behavior of $MAPbI_3$ in humidity differs substantially from that of $MAPbBr_3$, arising from differences in the composition-dependent formation and propagation of the hydrated perovskite phase. Our results show that the unique behavior of surface hydration in $MAPbI_3$ may benefit the optoelectronic properties of the perovskite films, suggesting that appropriate control of humidity during and after device preparation could lead to enhanced device performance. $MAPbBr_3$ shows better structural stability relative to its I-based counterpart but still requires careful encapsulation to ensure operational stability.

■ EXPERIMENTAL METHODS

Film Preparation. The perovskite films were deposited from a precursor solution containing methylammonium iodide/bromide (1 M) and lead iodide/bromide (1 M) in an anhydrous DMF:DMSO solution at 4:1 (v:v) ratio. The precursor solution was spin-coated onto soda-lime glass substrates at 4000 rpm for 30 s. At ~ 8 s after starting the process, 300 μL of diethyl ether was poured on the spinning substrate. The coated substrates were then annealed at 100 °C for 10 min in the nitrogen glovebox. The thickness of the films was ~ 350 nm, determined by cross-sectional SEM measurement.

General Characterization Methods. The optical absorption spectra were measured using a spectrometer (PerkinElmer Lambda 1050) in the range of 350−2000 nm. SEM images were obtained using a field emission electron microscope (Hitachi S-4800). XRD spectra were measured using an X-ray diffractometer (Rigaku Ultima III) in parallel beam mode with an incident angle of 1°, a step size of 0.02°, and a speed of 0.50° per minute.

In Situ PL Measurement. Perovskite films were kept inside of an airtight environmental chamber built with a 2.75 in. outside diameter conflat flange (Lesker) (Figure S4) for the controlled environment PL and TRPL measurements. The chamber was purged with a nitrogen carrier gas through a water bubbler at a flow rate of 0.083 m^3/min to maintain 80 ± 5% RH at the outlet of the environmental chamber. Samples were illuminated through the film side, and measurements were performed at room temperature. A 532 nm cw laser (beam diameter ~ 90 μm) at 91 mW/cm^2 and a 405 nm cw laser (beam diameter ~ 200 μm) at 528 mW/cm^2 were used to excite $MAPbI_3$ and $MAPbBr_3$ samples, respectively. The power densities were tested on the control samples in air to ensure no significant illumination damage during the measurement time. The PL signal was detected via a Symphony-II CCD (Horiba) detector after a 300 g/mm grating monochromator (integration time = 0.5 s). Steady-state PL spectra were taken at an interval of 1 min over a period of 5 h. The data was used to construct PL evolution maps.

In Situ TRPL Measurement. The same controlled environment apparatus was used for the TRPL measurements. The samples were excited by a 532 and 450 nm pulse laser (Fianium model SC400-2, pulse width ≈ 5 ps, beam diameter ≈ 150 μm) at an incident photon flux of 10^9 photons/(pulse·cm^2) for $MAPbI_3$ and $MAPbBr_3$ samples, respectively. TRPL measurements were performed with a time-correlated single-photon counting (TCSPC) module (Becker & Hickel Simple Tau SPCM 130-E/M module), and the PL signal was detected via a hybrid avalanche photodiode (APD) and photomultiplier tube (PMT) module (R10467U-50). TRPL measurements were performed continuously for 4 h. Integration times were 300 and 120 s for $MAPbI_3$ and $MAPbBr_3$, respectively.

In Situ Hall Effect Measurement. A modified Hall effect vacuum chamber (MMR Technologies) was used for controlled environment measurements using the same conditions as those in the PL/TRPL measurements. Perovskite films were laser patterned into a square shape (1 cm by 1 cm), and Au contacts were deposited in a Van der Pauw geometry (Figure S7). For the Hall effect measurement, the longitudinal current I was generated using a Keithley 2601 source meter by sweeping the voltage V from −20 to 20 V with a 30 s interval followed by a reversed scan (20 to −20 V) 5 s later. The transverse Hall voltage under a 0.26 T steady magnetic field generated by an electromagnet was monitored using a Keithley 6514 electrometer in the voltage. Carrier concentration was then calculated by using the equation $V_H = IB/nte$, where V_H is the transverse Hall voltage, B is the magnetic field, n is carrier density, t is the thickness of the film, and e is unit electron charge.

■ ASSOCIATED CONTENT

ⓢ Supporting Information

The Supporting Information is available free of charge on the ACS Publications website at DOI: 10.1021/acs.jpclett.8b02595.

Tauc plots of MAPbI$_3$ and MAPbBr$_3$; excitonic peak fitting for MAPbBr$_3$; biexponential fitting time constants and mean lifetimes; XRD spectra of pristine MAPbI$_3$ and MAPbBr$_3$; photo of the environmental chamber; PL spectra of MAPbI$_3$ and MAPbBr$_3$ in dry nitrogen; SEM images of pristine and degraded MAPbI$_3$ films; XRD spectra of degraded MAPbI$_3$ and MAPbBr$_3$ films; SEM images of pristine and degraded MAPbBr$_3$ films; and photo and schematic image of the Hall effect measurement setup (PDF)

■ AUTHOR INFORMATION

Corresponding Author
*E-mail: Michael.Heben@utoledo.edu.
ORCID ●
Zhaoning Song: 0000-0002-6677-0994
Suneth C. Watthage: 0000-0001-8728-9561
Randy J. Ellingson: 0000-0001-9520-6586
Michael J. Heben: 0000-0002-3788-3471

Author Contributions
[#]Z.S. and N.S. contributed equally to this work.

Notes
The authors declare no competing financial interest.

■ ACKNOWLEDGMENTS

■ REFERENCES

(1) NREL Solar Cell Efficiency Chart. https://www.nrel.gov/pv/assets/images/efficiency-chart-20180716.jpg (accessed Aug 6, 2018).

(2) Snaith, H. J. Perovskites: The Emergence of a New Era for Low-Cost, High-Efficiency Solar Cells. *J. Phys. Chem. Lett.* **2013**, 4, 3623−3630.

(3) Green, M. A.; Ho-Baillie, A.; Snaith, H. J. The emergence of perovskite solar cells. *Nat. Photonics* **2014**, 8, 506−514.

(4) Yin, W.-J.; Yang, J.-H.; Kang, J.; Yan, Y.; Wei, S.-H. Halide perovskite materials for solar cells: a theoretical review. *J. Mater. Chem. A* **2015**, 3, 8926−8942.

(5) Song, Z.; Watthage, S. C.; Phillips, A. B.; Heben, M. J. Pathways toward high-performance perovskite solar cells: review of recent advances in organo-metal halide perovskites for photovoltaic applications. *J. Photonics Energy* **2016**, 6, 022001.

(6) Eperon, G. E.; Leijtens, T.; Bush, K. A.; Prasanna, R.; Green, T.; Wang, J. T.-W.; McMeekin, D. P.; Volonakis, G.; Milot, R. L.; May, R.; et al. Perovskite-perovskite tandem photovoltaics with optimized band gaps. *Science* **2016**, 354, 861−865.

(7) Correa-Baena, J.-P.; Abate, A.; Saliba, M.; Tress, W.; Jesper Jacobsson, T.; Gratzel, M.; Hagfeldt, A. The rapid evolution of highly efficient perovskite solar cells. *Energy Environ. Sci.* **2017**, 10, 710−727.

(8) Zhao, D.; Yu, Y.; Wang, C.; Liao, W.; Shrestha, N.; Grice, C. R.; Cimaroli, A. J.; Guan, L.; Ellingson, R. J.; Zhu, K.; et al. Low-bandgap mixed tin−lead iodide perovskite absorbers with long carrier lifetimes for all-perovskite tandem solar cells. *Nat. Energy* **2017**, 2, 17018.

(9) Celik, I.; Phillips, A. B.; Song, Z.; Yan, Y.; Ellingson, R. J.; Heben, M. J.; Apul, D. Environmental analysis of perovskites and other relevant solar cell technologies in a tandem configuration. *Energy Environ. Sci.* **2017**, 10, 1874−1884.

(10) Sahli, F.; Werner, J.; Kamino, B. A.; Bräuninger, M.; Monnard, R.; Paviet-Salomon, B.; Barraud, L.; Ding, L.; Diaz Leon, J. J.; Sacchetto, D.; et al. Fully textured monolithic perovskite/silicon tandem solar cells with 25.2% power conversion efficiency. *Nat. Mater.* **2018**, 17, 820−826.

(11) Park, N.-G.; Grätzel, M.; Miyasaka, T.; Zhu, K.; Emery, K. Towards stable and commercially available perovskite solar cells. *Nat. Energy* **2016**, 1, 16152.

(12) Snaith, H. J. Present status and future prospects of perovskite photovoltaics. *Nat. Mater.* **2018**, 17, 372−376.

(13) Song, Z.; McElvany, C. L.; Phillips, A. B.; Celik, I.; Krantz, P. W.; Watthage, S. C.; Liyanage, G. K.; Apul, D.; Heben, M. J. A technoeconomic analysis of perovskite solar module manufacturing with low-cost materials and techniques. *Energy Environ. Sci.* **2017**, 10, 1297−1305.

(14) Chang, N. L.; Yi Ho-Baillie, A. W.; Basore, P. A.; Young, T. L.; Evans, R.; Egan, R. J. A manufacturing cost estimation method with uncertainty analysis and its application to perovskite on glass photovoltaic modules. *Prog. Photovoltaics* **2017**, 25, 390−405.

(15) Snaith, H. J.; Hacke, P. Enabling reliability assessments of pre-commercial perovskite photovoltaics with lessons learned from industrial standards. *Nat. Energy* **2018**, 3, 459−465.

(16) Leijtens, T.; Eperon, G. E.; Noel, N. K.; Habisreutinger, S. N.; Petrozza, A.; Snaith, H. J. Stability of Metal Halide Perovskite Solar Cells. *Adv. Energy Mater.* **2015**, 5, 1500963.

(17) Tiep, N. H.; Ku, Z.; Fan, H. J. Recent Advances in Improving the Stability of Perovskite Solar Cells. *Adv. Energy Mater.* **2016**, 6, 1501420.

(18) Wang, D.; Wright, M.; Elumalai, N. K.; Uddin, A. Stability of perovskite solar cells. *Sol. Energy Mater. Sol. Cells* **2016**, 147, 255−275.

(19) Berhe, T. A.; Su, W.-N.; Chen, C.-H.; Pan, C.-J.; Cheng, J.-H.; Chen, H.-M.; Tsai, M.-C.; Chen, L.-Y.; Dubale, A. A.; Hwang, B.-J. Organometal halide perovskite solar cells: degradation and stability. *Energy Environ. Sci.* **2016**, 9, 323−356.

(20) Yang, J.; Kelly, T. L. Decomposition and Cell Failure Mechanisms in Lead Halide Perovskite Solar Cells. *Inorg. Chem.* **2017**, 56, 92−101.

(21) Han, Y.; Meyer, S.; Dkhissi, Y.; Weber, K.; Pringle, J. M.; Bach, U.; Spiccia, L.; Cheng, Y.-B. Degradation observations of encapsulated planar CH$_3$NH$_3$PbI$_3$ perovskite solar cells at high temperatures and humidity. *J. Mater. Chem. A* **2015**, 3, 8139−8147.

(22) Kulbak, M.; Gupta, S.; Kedem, N.; Levine, I.; Bendikov, T.; Hodes, G.; Cahen, D. Cesium Enhances Long-Term Stability of Lead Bromide Perovskite-Based Solar Cells. *J. Phys. Chem. Lett.* **2016**, 7, 167−172.

(23) Aristidou, N.; Sanchez-Molina, I.; Chotchuangchutchaval, T.; Brown, M.; Martinez, L.; Rath, T.; Haque, S. A. The Role of Oxygen in the Degradation of Methylammonium Lead Trihalide Perovskite Photoactive Layers. *Angew. Chem., Int. Ed.* **2015**, 54, 8208−8212.

(24) Yu, X.; Qin, Y.; Peng, Q. Probe Decomposition of Methylammonium Lead Iodide Perovskite in N$_2$ and O$_2$ by in Situ Infrared Spectroscopy. *J. Phys. Chem. A* **2017**, 121, 1169−1174.

(25) Pearson, A. J.; Eperon, G. E.; Hopkinson, P. E.; Habisreutinger, S. N.; Wang, J. T.-W.; Snaith, H. J.; Greenham, N. C. Oxygen Degradation in Mesoporous Al$_2$O$_3$/CH$_3$NH$_3$PbI$_{3-x}$Cl$_x$ Perovskite Solar Cells: Kinetics and Mechanisms. *Adv. Energy Mater.* **2016**, 6, 1600014.

(26) Leijtens, T.; Eperon, G. E.; Pathak, S.; Abate, A.; Lee, M. M.; Snaith, H. J. Overcoming ultraviolet light instability of sensitized TiO$_2$ with meso-superstructured organometal tri-halide perovskite solar cells. *Nat. Commun.* **2013**, 4, 3885.

(27) Misra, R. K.; Ciammaruchi, L.; Aharon, S.; Mogilyansky, D.; Etgar, L.; Visoly-Fisher, I.; Katz, E. A. Effect of Halide Composition on the Photochemical Stability of Perovskite Photovoltaic Materials. *ChemSusChem* **2016**, 9, 2572−2577.

(28) Song, Z.; Wang, C.; Phillips, A. B.; Grice, C. R.; Zhao, D.; Yu, Y.; Chen, C.; Li, C.; Yin, X.; Ellingson, R. Probing the Origins of Photodegradation in Organic−Inorganic Metal Halide Perovskites

with Time-Resolved Mass Spectrometry. *Sustainable Energy & Fuels* **2018**, DOI: 10.1039/C8SE00358K.

(29) Divitini, G.; Cacovich, S.; Matteocci, F.; Cinà, L.; Di Carlo, A.; Ducati, C. In situ observation of heat-induced degradation of perovskite solar cells. *Nat. Energy* **2016**, *1*, 15012.

(30) Akbulatov, A. F.; Luchkin, S. Y.; Frolova, L. A.; Dremova, N. N.; Gerasimov, K. L.; Zhidkov, I. S.; Anokhin, D. V.; Kurmaev, E. Z.; Stevenson, K. J.; Troshin, P. A. Probing the Intrinsic Thermal and Photochemical Stability of Hybrid and Inorganic Lead Halide Perovskites. *J. Phys. Chem. Lett.* **2017**, *8*, 1211−1218.

(31) Domanski, K.; Correa-Baena, J.-P.; Mine, N.; Nazeeruddin, M. K.; Abate, A.; Saliba, M.; Tress, W.; Hagfeldt, A.; Grätzel, M. Not All That Glitters Is Gold: Metal-Migration-Induced Degradation in Perovskite Solar Cells. *ACS Nano* **2016**, *10*, 6306−6314.

(32) Kato, Y.; Ono, L. K.; Lee, M. V.; Wang, S.; Raga, S. R.; Qi, Y. Silver Iodide Formation in Methyl Ammonium Lead Iodide Perovskite Solar Cells with Silver Top Electrodes. *Adv. Mater. Interfaces* **2015**, *2*, 1500195.

(33) Besleaga, C.; Abramiuc, L. E.; Stancu, V.; Tomulescu, A. G.; Sima, M.; Trinca, L.; Plugaru, N.; Pintilie, L.; Nemnes, G. A.; Iliescu, M.; et al. Iodine Migration and Degradation of Perovskite Solar Cells Enhanced by Metallic Electrodes. *J. Phys. Chem. Lett.* **2016**, *7*, 5168−5175.

(34) Wang, S.; Jiang, Y.; Juarez-Perez, E. J.; Ono, L. K.; Qi, Y. Accelerated degradation of methylammonium lead iodide perovskites induced by exposure to iodine vapour. *Nat. Energy* **2017**, *2*, 16195.

(35) Domanski, K.; Roose, B.; Matsui, T.; Saliba, M.; Turren-Cruz, S.-H.; Correa-Baena, J.-P.; Carmona, C. R.; Richardson, G.; Foster, J. M.; De Angelis, F.; et al. Migration of cations induces reversible performance losses over day/night cycling in perovskite solar cells. *Energy Environ. Sci.* **2017**, *10*, 604−613.

(36) Christians, J. A.; Miranda Herrera, P. A.; Kamat, P. V. Transformation of the Excited State and Photovoltaic Efficiency of $CH_3NH_3PbI_3$ Perovskite upon Controlled Exposure to Humidified Air. *J. Am. Chem. Soc.* **2015**, *137*, 1530−1538.

(37) Leguy, A. M. A.; Hu, Y.; Campoy-Quiles, M.; Alonso, M. I.; Weber, O. J.; Azarhoosh, P.; van Schilfgaarde, M.; Weller, M. T.; Bein, T.; Nelson, J.; et al. Reversible Hydration of $CH_3NH_3PbI_3$ in Films, Single Crystals, and Solar Cells. *Chem. Mater.* **2015**, *27*, 3397−3407.

(38) Song, Z.; Abate, A.; Watthage, S. C.; Liyanage, G. K.; Phillips, A. B.; Steiner, U.; Gratzel, M.; Heben, M. J. Perovskite Solar Cell Stability in Humid Air: Partially Reversible Phase Transitions in the PbI_2-CH_3NH_3I-H_2O System. *Adv. Energy Mater.* **2016**, *6*, 1600846.

(39) Frost, J. M.; Butler, K. T.; Brivio, F.; Hendon, C. H.; van Schilfgaarde, M.; Walsh, A. Atomistic Origins of High-Performance in Hybrid Halide Perovskite Solar Cells. *Nano Lett.* **2014**, *14*, 2584−2590.

(40) Yang, J.; Siempelkamp, B. D.; Liu, D.; Kelly, T. L. Investigation of $CH_3NH_3PbI_3$ Degradation Rates and Mechanisms in Controlled Humidity Environments Using in Situ Techniques. *ACS Nano* **2015**, *9*, 1955−1963.

(41) Huang, W.; Manser, J. S.; Kamat, P. V.; Ptasinska, S. Evolution of Chemical Composition, Morphology, and Photovoltaic Efficiency of $CH_3NH_3PbI_3$ Perovskite under Ambient Conditions. *Chem. Mater.* **2016**, *28*, 303−311.

(42) Li, D.; Bretschneider, S. A.; Bergmann, V. W.; Hermes, I. M.; Mars, J.; Klasen, A.; Lu, H.; Tremel, W.; Mezger, M.; Butt, H.-J.; et al. Humidity-Induced Grain Boundaries in $MAPbI_3$ Perovskite Films. *J. Phys. Chem. C* **2016**, *120*, 6363−6368.

(43) Zhu, Z.; Hadjiev, V. G.; Rong, Y.; Guo, R.; Cao, B.; Tang, Z.; Qin, F.; Li, Y.; Wang, Y.; Hao, F.; et al. Interaction of Organic Cation with Water Molecule in Perovskite $MAPbI_3$: From Dynamic Orientational Disorder to Hydrogen Bonding. *Chem. Mater.* **2016**, *28*, 7385−7393.

(44) Motti, S. G.; Gandini, M.; Barker, A. J.; Ball, J. M.; Srimath Kandada, A. R.; Petrozza, A. Photoinduced Emissive Trap States in Lead Halide Perovskite Semiconductors. *ACS Energy Lett.* **2016**, *1*, 726−730.

(45) Anaya, M.; Galisteo-López, J. F.; Calvo, M. E.; Espinós, J. P.; Míguez, H. Origin of Light-Induced Photophysical Effects in Organic Metal Halide Perovskites in the Presence of Oxygen. *J. Phys. Chem. Lett.* **2018**, *9*, 3891−3896.

(46) Saidaminov, M. I.; Abdelhady, A. L.; Murali, B.; Alarousu, E.; Burlakov, V. M.; Peng, W.; Dursun, I.; Wang, L.; He, Y.; Maculan, G.; et al. High-quality bulk hybrid perovskite single crystals within minutes by inverse temperature crystallization. *Nat. Commun.* **2015**, *6*, 7586.

(47) Wu, B.; Nguyen, H. T.; Ku, Z.; Han, G.; Giovanni, D.; Mathews, N.; Fan, H. J.; Sum, T. C. Discerning the Surface and Bulk Recombination Kinetics of Organic−Inorganic Halide Perovskite Single Crystals. *Adv. Energy Mater.* **2016**, *6*, 1600551.

(48) Wenger, B.; Nayak, P. K.; Wen, X.; Kesava, S. V.; Noel, N. K.; Snaith, H. J. Consolidation of the optoelectronic properties of $CH_3NH_3PbBr_3$ perovskite single crystals. *Nat. Commun.* **2017**, *8*, 590.

(49) Tanaka, K.; Takahashi, T.; Ban, T.; Kondo, T.; Uchida, K.; Miura, N. Comparative study on the excitons in lead-halide-based perovskite-type crystals $CH_3NH_3PbBr_3$ $CH_3NH_3PbI_3$. *Solid State Commun.* **2003**, *127*, 619−623.

(50) Yang, Y.; Yan, Y.; Yang, M.; Choi, S.; Zhu, K.; Luther, J. M.; Beard, M. C. Low surface recombination velocity in solution-grown $CH_3NH_3PbBr_3$ perovskite single crystal. *Nat. Commun.* **2015**, *6*, 7961.

(51) Chen, S.; Hou, Y.; Chen, H.; Richter, M.; Guo, F.; Kahmann, S.; Tang, X.; Stubhan, T.; Zhang, H.; Li, N.; et al. Exploring the Limiting Open-Circuit Voltage and the Voltage Loss Mechanism in Planar $CH_3NH_3PbBr_3$ Perovskite Solar Cells. *Adv. Energy Mater.* **2016**, *6*, 1600132.

(52) Elliott, R. J. Intensity of Optical Absorption by Excitons. *Phys. Rev.* **1957**, *108*, 1384−1389.

(53) Saba, M.; Cadelano, M.; Marongiu, D.; Chen, F.; Sarritzu, V.; Sestu, N.; Figus, C.; Aresti, M.; Piras, R.; Geddo Lehmann, A.; et al. Correlated electron−hole plasma in organometal perovskites. *Nat. Commun.* **2014**, *5*, 5049.

(54) Stranks, S. D.; Eperon, G. E.; Grancini, G.; Menelaou, C.; Alcocer, M. J. P.; Leijtens, T.; Herz, L. M.; Petrozza, A.; Snaith, H. J. Electron-Hole Diffusion Lengths Exceeding 1 Micrometer in an Organometal Trihalide Perovskite Absorber. *Science* **2013**, *342*, 341−344.

(55) Zhou, W.; Zhao, Y.; Shi, C.; Huang, H.; Wei, J.; Fu, R.; Liu, K.; Yu, D.; Zhao, Q. Reversible Healing Effect of Water Molecules on Fully Crystallized Metal−Halide Perovskite Film. *J. Phys. Chem. C* **2016**, *120*, 4759.

(56) Müller, C.; Glaser, T.; Plogmeyer, M.; Sendner, M.; Döring, S.; Bakulin, A. A.; Brzuska, C.; Scheer, R.; Pshenichnikov, M. S.; Kowalsky, W.; et al. Water Infiltration in Methylammonium Lead Iodide Perovskite: Fast and Inconspicuous. *Chem. Mater.* **2015**, *27*, 7835−7841.

(57) Mosconi, E.; Azpiroz, J. M.; De Angelis, F. Ab Initio Molecular Dynamics Simulations of Methylammonium Lead Iodide Perovskite Degradation by Water. *Chem. Mater.* **2015**, *27*, 4885−4892.

(58) Long, R.; Fang, W.; Prezhdo, O. V. Moderate Humidity Delays Electron−Hole Recombination in Hybrid Organic−Inorganic Perovskites: Time-Domain Ab Initio Simulations Rationalize Experiments. *J. Phys. Chem. Lett.* **2016**, *7*, 3215−3222.

(59) Li, Y.; Xu, X.; Wang, C.; Wang, C.; Xie, F.; Yang, J.; Gao, Y. Degradation by Exposure of Coevaporated $CH_3NH_3PbI_3$ Thin Films. *J. Phys. Chem. C* **2015**, *119*, 23996−24002.

(60) Berweger, S.; MacDonald, G. A.; Yang, M.; Coakley, K. J.; Berry, J. J.; Zhu, K.; DelRio, F. W.; Wallis, T. M.; Kabos, P. Electronic and Morphological Inhomogeneities in Pristine and Deteriorated Perovskite Photovoltaic Films. *Nano Lett.* **2017**, *17*, 1796−1801.

(61) Song, Z.; Werner, J.; Shrestha, N.; Sahli, F.; De Wolf, S.; Niesen, B.; Watthage, S. C.; Phillips, A. B.; Ballif, C.; Ellingson, R. J.; et al. Probing Photocurrent Nonuniformities in the Subcells of Monolithic Perovskite/Silicon Tandem Solar Cells. *J. Phys. Chem. Lett.* **2016**, *7*, 5114−5120.

(62) Song, Z.; Werner, J.; Watthage, S. C.; Sahli, F.; Shrestha, N.; De Wolf, S.; Niesen, B.; Phillips, A. B.; Ballif, C.; Ellingson, R. J.; et al.

Imaging the Spatial Evolution of Degradation in Perovskite/Si Tandem Solar Cells After Exposure to Humid Air. *IEEE J. Photovol.* **2017**, *7*, 1563−1568.

(63) Eperon, G. E.; Habisreutinger, S. N.; Leijtens, T.; Bruijnaers, B. J.; van Franeker, J. J.; deQuilettes, D. W.; Pathak, S.; Sutton, R. J.; Grancini, G.; Ginger, D. S.; et al. The Importance of Moisture in Hybrid Lead Halide Perovskite Thin Film Fabrication. *ACS Nano* **2015**, *9*, 9380−9393.

(64) Petrus, M. L.; Hu, Y.; Moia, D.; Calado, P.; Leguy, A. M. A.; Barnes, P. R. F.; Docampo, P. The Influence of Water Vapor on the Stability and Processing of Hybrid Perovskite Solar Cells Made from Non-Stoichiometric Precursor Mixtures. *ChemSusChem* **2016**, *9*, 2699−2707.

(65) Wang, B.; Zhang, Z.-G.; Ye, S.; Rao, H.; Bian, Z.; Huang, C.; Li, Y. Room-temperature water-vapor annealing for high-performance planar perovskite solar cells. *J. Mater. Chem. A* **2016**, *4*, 17267−17273.

(66) Grancini, G.; D'Innocenzo, V.; Dohner, E. R.; Martino, N.; Srimath Kandada, A. R.; Mosconi, E.; De Angelis, F.; Karunadasa, H. I.; Hoke, E. T.; Petrozza, A. $CH_3NH_3PbI_3$ perovskite single crystals: surface photophysics and their interaction with the environment. *Chem. Sci.* **2015**, *6*, 7305−7310.